Spatial Characteristics of Functional and Non-functional Satellites in Low Earth Orbit

Vishnu Anand Muruganandan [(1)] *, Richard Clare [(1)], Andrew Lambert [(2)], Steve Weddell[1]

[(1)] Department of Electrical & Computer Engineering, University of Canterbury, New Zealand
[(2)] School of Electrical and Information Technology, UNSW, Canberra, Australia
**Email:vishnuanand.muruganandan@canterbury.ac.nz*

ABSTRACT

The functional and non-functional satellites in Low Earth Orbit (LEO) are imaged without motion blur. The images are post-processed using a novel algorithm to obtain the length, width, and orientation of the major axis of the satellites. The estimated length and width of the satellites agree with the true dimension and the estimated orientation of non-functional satellites changes rapidly whereas the orientation of the functional satellite is relatively stable in each frame. Hence, this novel image processing algorithm is effective in estimating the dimension of asymmetric objects (satellites and debris) and characterise the non-functional satellites in LEO.

1 Introduction

The derelict objects (non-functional payloads and rocket boosters) in Low Earth Orbit (LEO) have been increasing exponentially. As of 2019, there are 2987 derelict objects and 1250 functioning payloads in LEO. The LEO has the most derelict mass per volume and functional payloads. This scenario is a threat to functional payloads and human missions in LEO. Hence it is important to characterise the non-functional payload in LEO [1].

In this paper, the spatial characteristics of three non-functional payloads (ALOS-1, ERS-2, SEASAT) and a functional payload (ISS) are estimated using optical observation. Advanced Land Observing Satellite (ALOS-1) was launched into LEO in 2006 and it became non-functional after five years [2]. Earth Remote Sensing Satellite (ERS-2) was launched into LEO in 1996 and it became non-functional by 2011 [3]. Seafaring satellite (SEASAT) was launched into LEO in 1978 and it became non-functional after 110 days of operation [4].

In section 2 operation of the optical telescope, detector, and observation method are described. In section 3 the novel image processing algorithm is described and an estimate of the length, width, and orientation of the major axis of satellites (ISS, ALOS-1, ERS-2, and SEASAT) are provided. In section 4 the results and future works are discussed.

2 Background

The Boller and Chivens (B&C) telescope at the University of Canterbury Mount John Observatory (UCMJO) is used for imaging artificial satellites at Low Earth Orbit (LEO). The primary aperture and focal length of B&C are 0.61 m and 3.85 m respectively. The detector (FLIR GS3) has a sensor width of 11.3mm and a pixel width of 5.5µm. In a Field of View (FoV) of 10 arcminutes, the target is captured over 8 to 12 frames based on its range. The FoV of a telescope at infinite distance is calculated using Eq.1 but Eq.2 provides the accurate sampling distance for finite distance,

$$FoV = \tan^{-1}\frac{F}{S} \quad (1)$$

$$SD_{sw} = \frac{S \times R}{F} \quad (2)$$

SD_{sw} is the sampling distance for the sensor width, F is the focal length of the telescope, S is the physical width of the sensor, and R is the slanting distance between the telescope and the satellite. Eq.3 provides the time (t) required for the satellite to move across the sampling distance,

$$t = \frac{SD_{sw}}{V} \quad (3)$$

Where V is the orbital velocity of the satellite. For example, when ISS at an altitude of 435 km and elevation of 44°, the slanting distance between the telescope and the ISS is 603 km. Then the GS3 image sensor covers a sampling distance of 1.8 km at an altitude of 435 km. The time taken for the ISS to cross the sampling distance of 1.8 km is 0.23 s.

The B&C telescope does not have satellite tracking capability. Hence, the telescope is pointed to a star that has closer proximity to the trajectory of the satellite, and during the estimated time of contact, multiple frames with satellite images are captured and the number of frames captured is estimated using Eq.4.

$$No.of\ frames = P \times t \quad (4)$$

P is the frame rate of the camera, using GS3 with 50 frames/s and time of 0.23 s, the ISS is captured in 12

frames. The SD_{pw} of one pixel is estimated using E.q.5. Where SD_{pw} is the sampling distance of the pixel width, and (P) is the width of a pixel. For example, when the ISS is at an elevation of 44°, the spatial resolution or sampling distance of a pixel is 86 cm.

$$SD_{pw} = \frac{P \times R}{F} \quad (5)$$

Theoretically, the spatial resolution of 86 cm is achievable but it is not achievable in practice. During the optical observation, the spatial resolution of the image is degraded due to motion blur and atmospheric turbulence. In our previous publication [5], motion blur had a primary effect on image resolution. Since B&C doesn't have a tracking system, it is essential to image the satellite without motion blur. Eq.7 provides the required exposure time (t_e) to image the target without motion blur.

$$SD_{pw} = V \times t_e \quad (6)$$

Substituting Eq.6 in Eq.5 gives Eq.7

$$t_e = \frac{P}{F} \times \frac{R}{V} \quad (7)$$

For example, when the ISS at an elevation of 44°, the required exposure time for GS3 on the B&C to image the ISS without motion blur is 0.23 ms. This exposure time denotes the time taken for the ISS to cross a pixel width.

3 Spatial Characterisation

In this paper, the satellites at LEO are imaged without motion blur, but image blur due to atmospheric turbulence is not removed. The authors suggest the readers read the article [5] which covers the post-processing methodology to remove atmospheric blur. The physical dimension (length and width), and orientation of the major axis of the satellite in LEO are estimated by the following steps:

i) Local threshold is estimated by averaging the pixel values in the region, and pixels with intensity above the threshold value are extracted from the raw image. The extracted pixels are grouped using the nearest neighbour search and if the size (number of pixels) of the group is between 36 to 6000 then it is identified as an object which is shown in the (left) fig.2.

ii) The pixels along the perimeter of that object are labeled and the two farthest pixels in the perimeter are identified.

iii) The distance between the two farthest pixels is the length (major axis) of the object. The major axis is shown in the red line on the (right) fig.2.

iv) The perpendicular distance at the midpoint of the major axis is the width of the target. The minor axis is shown in the blue line on the (right) fig.2.

v) The average width of the target is estimated by dividing the total number of pixels in the target by the length of the target (pixels).

vi) The Spatial Resolution (SR) of one pixel is estimated based on Eq.5 and for example, SR of the object in fig.2 is 0.86 m and SR is used to estimate the length and width of the target in meters, which is shown in fig.3.

vii) The angle between the major axis of the target and the x-axis is the orientation of the target, which is shown in fig.3.

3.1 ISS

The ISS in fig.2 is imaged on 2020-10-31 (UTC) 08:58:37. During the observation, the apparent magnitude of the ISS is -3.5, elevation is 44°, slanting distance (R) is 603 km, and required exposure time is 0.23 ms. The true length and width of the ISS are 109m and 51m respectively [6].

For two reasons, the telescope is pointed to the star (HIP90414) which is closer to the trajectory of the ISS. First, the star helps in reducing the pointing error of the telescope. If the location of the star in FoV has an offset, then the star is reset to the center of FoV. Second, the Point Spread Function (PSF) of a star can be used to estimate the atmospheric turbulence and restore the image. But in this case, the exposure time is very low to detect the PSF of a star. Based on the apparent magnitude of the star, an exposure time of more than one second is required to obtain the PSF of a star.

The length (red line), width (blue line) and orientation of the major axis of the ISS shown in fig.2 (right) are 110.2m, 49.5m, and -28° respectively. Fig. 3 shows the estimated length, and the width of the ISS compared with the true length and width. The images are taken with 8bit mode, hence the intensity value of a pixel varies from 0 to 255 units. In fig.3 the threshold value in all frames remains constant (18 units) except the 6th frame where the background noise is estimated to be 20 units. The sharp decrease in the length and width of the ISS at the 6th frame is due to an increase in threshold value.

Figure 1. CAD model of ISS. [7]

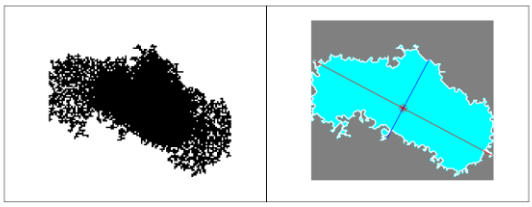

Figure 2. (left) ISS extraction, (right) length, width, and orientation of ISS.

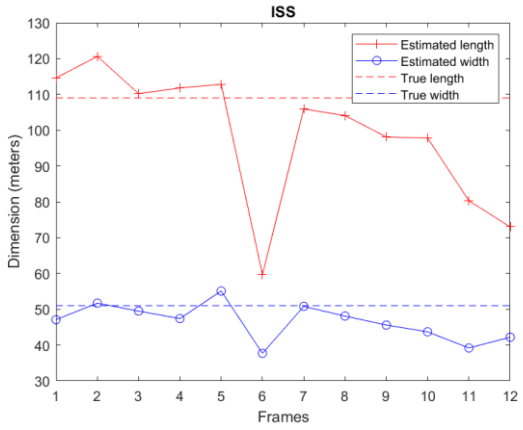

Figure 3. Estimation of length and width of ISS compared to the true dimension vs the captured frames.

In fig.3 the estimated length of the ISS agrees with the true length at frame 3 and the estimated width of the ISS agrees with the true width at frame 2. Fig. 4 shows the orientation of the ISS over 12 frames. Since, the ISS is functional in LEO the change in orientation between frames is within 4 degrees except between frames 2 and 3, where the variation is around 15 degrees. This sudden change between frames 2 and 3 may be due to the effect of noise in the image or a change in the attitude of ISS in orbit. Since the ISS is functional the estimated orientation over 12 frames is relatively stable.

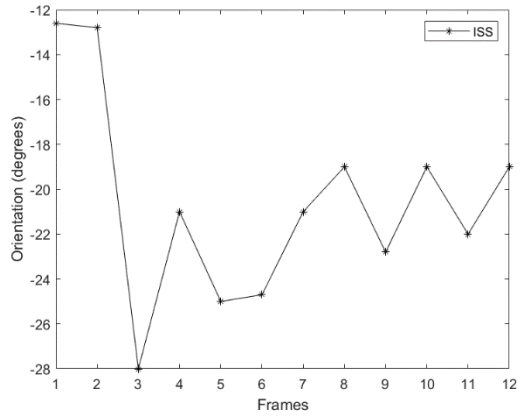

Figure 4. Orientation of the major axis of ISS vs the captured frames.

3.2 ALOS-1

The ALOS-1 in fig.6 is imaged on 2020-09-15 (UTC) 16:28:32. During the observation, the apparent magnitude of ALOS-1 is 2.3, elevation is 84°, slanting distance (R) is 704 km, and required exposure time is 0.27 ms. The telescope is pointed to the star (HIP18635) which is closer to the trajectory of ALOS-1. The true length and width of ALOS-1 are 27.4m (including the length of solar panel) and 9m respectively [2]. The threshold value for the first 8 frames and last 4 frames are 42 units and 43 units respectively.

The length (red line), width (blue line) and orientation of the major axis of the ISS shown in fig.6 (right) are 27.8m, 21.1m, and 40.6° respectively. In fig.7 estimated the length of ALOS-1at frames 3 and 4 agrees with the true length of ALOS-1 but the estimated width is 12m higher than the true width. Because the true width is based on the 2-d image but in the observed image, the height (3d) of ALOS-1 might be illuminated, which adds more width in the estimation.

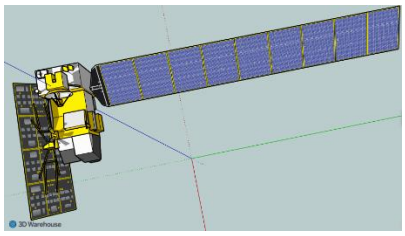

Figure 5. CAD model of ALOS-1. [8]

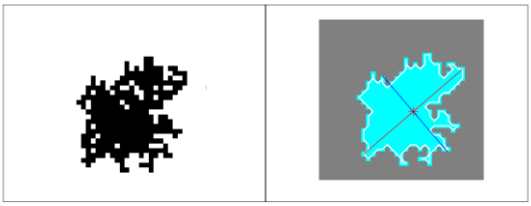

Figure 6. (left) ALOS-1 extraction, (right) length, width, and orientation of ALOS-1.

In this case, the average width of the object would give better results. The average width of the object is estimated using Eq.8. The area is the number of pixels in the object and length is the number of pixels along the major axis. The average width of ALOS-1 in fig.6 is 10.8 m which is closer to the true width of 9 m.

$$Average\ width = \frac{Area}{length} \qquad (8)$$

In this novel image processing algorithm, the estimation of the length (major axis) of the satellite has better

accuracy than the width because the width (minor axis) is estimated at the midpoint of the major axis, and the true width of the satellite doesn't have to be uniform over its entire length.

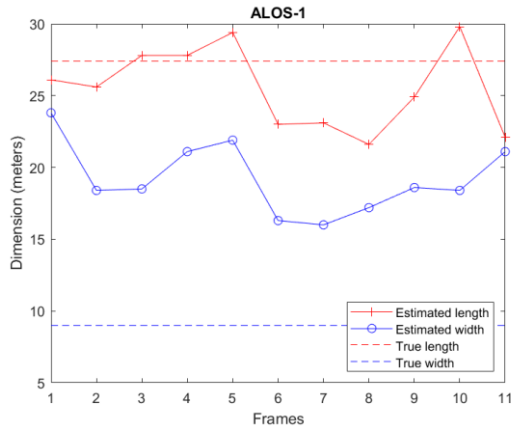

Figure 7. Estimation of length and width of ALOS-1 compared to the true dimension vs the captured frames.

Fig. 8 shows the orientation of ALOS-1 over 11 frames. Since ALOS-1 is a non-functional satellite the change in orientation is highly unstable. The maximum and minimum change in orientation between frames are 120° and 20° respectively. This might be due to the increased rotational velocity or tumbling of the satellite on a shorter axis.

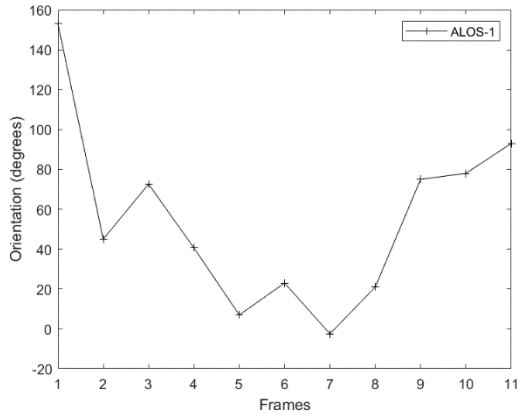

Figure 8. Orientation of the major axis of ALOS-1 vs the captured frames.

3.3 ERS-2

The ERS-2 in fig.10 is imaged on 2020-09-15 (UTC) 17:50:58. During the observation, the apparent magnitude of ERS-2 is 1.8, elevation is 76°, slanting distance (R) is 527 km, and required exposure time is 0.2 ms. The telescope is pointed to the star (HIP27317) which is closer to the trajectory of ERS-2. The true length and width of ERS-2 are 11.8 m (including the length of solar panel) and 11.7 m respectively [3].

The length (red line) and width (blue line) and orientation of the major axis of ERS-2 show in fig.10 (right) are 14.7m, 9.5m, and 14.5° respectively. In fig.11, the estimated length of ERS-2 agrees with the true length at frames 4 and 7. At frame 2, the estimated width of ERS-2 is closer to the true width. The threshold value for ERS-2 is 43and 44 units.

Figure 9. CAD model of ERS-2. [9]

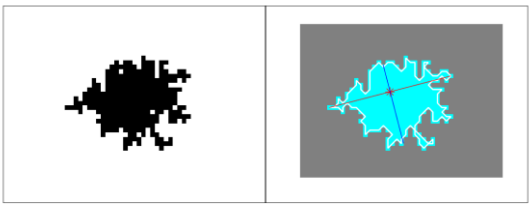

Figure 10. (left) ERS-2 extraction, (right) length, width, and orientation of ERS-2.

Fig. 12 shows the orientation of ERS-2 over 12 frames. Since ERS-2 is a non-functional satellite, the maximum and minimum change in orientation between frames is 100° and 10° respectively. The orientation of this derelict satellite in fig.12 varies relatively higher when compared to the orientation curve of the ISS in fig.4.

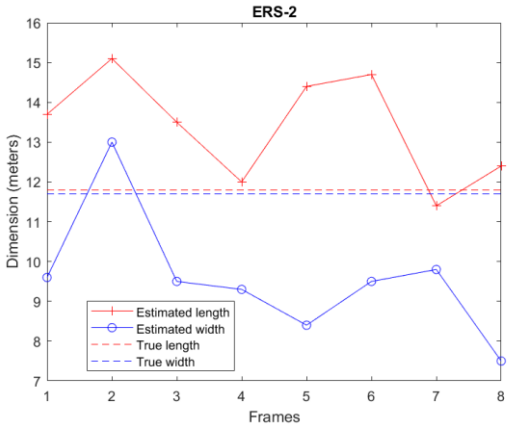

Figure 11. Estimation of length and width of ERS-2 compared to the true dimension vs the captured frames.

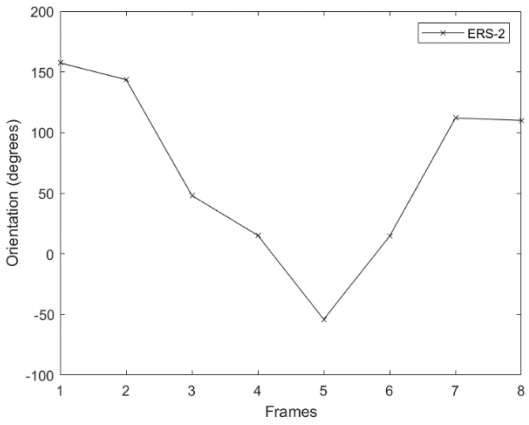

Figure 12. Orientation of the major axis of ERS-2 vs the captured frames.

3.4 SEASAT

The SEASAT in fig.14 is imaged on 2020-09-15 (UTC) 17:15:05. The apparent magnitude of SEASAT is 2.6, elevation is 59°, slanting distance (R) is 869 km, and required exposure time is 0.34 ms. The telescope is pointed to a star (HIP18428) which is closer to the trajectory of SEASAT. The true length and width of SEASAT are 21m and 14.5m (including the solar panel) respectively [4].

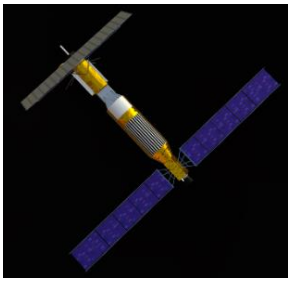

Figure 13. CAD model of SEASAT. [10]

The length (red line), width (blue line), and orientation of the major axis of SEASAT shown in fig.14 (right) are 21.1 m, 15.7 m, and -45° respectively. In fig.15, the estimated length of SEASAT agrees with the true length at frames 2 and the estimated width of SEASAT at frame 8 agrees with true width. The threshold value for SEASAT is 43 and 44 units.

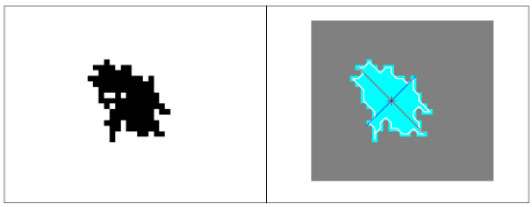

Figure 14. (left) SEASAT extraction, (right) length, width, and orientation of SEASAT.

Fig. 16 shows the change in orientation SEASAT over 12 frames. Since SEASAT is a non-functional satellite the maximum and minimum change in orientation of SESAT between frames is 100° and 10° respectively. Since SESAT is a derelict satellite, the rotational velocity of the satellite might be increased over years or the satellite might be tumbling at a higher rate. These characteristics of the non-functional satellite are reflected in fig.16, which shows relatively higher change in the orientation.

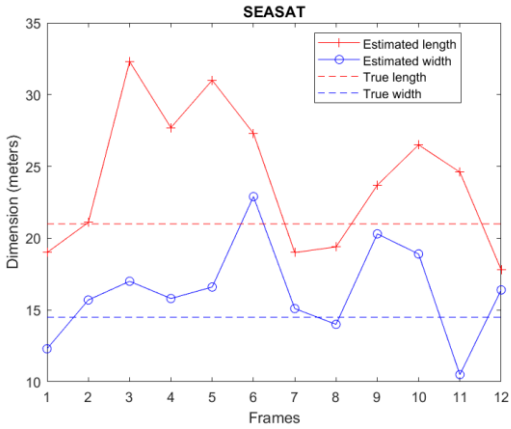

Figure 15. Estimation of length and width of SEASAT compared to the true dimension vs the captured frames.

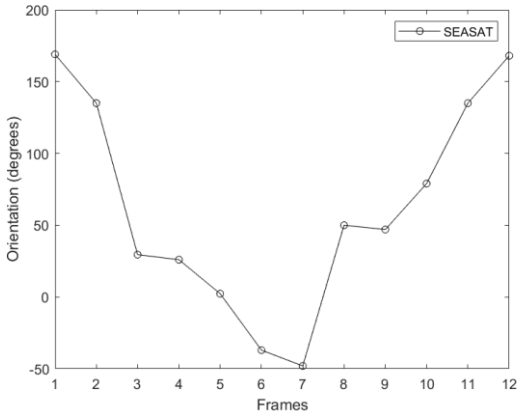

Figure 16. Orientation of the major axis of SEASAT vs the captured frames.

4 Conclusion

The novel image processing method is used to estimate the length and width of the satellites which agrees with the true dimension of the satellites. This shows that spatial characteristics of objects in LEO can be estimated if the object is imaged without motion blur.

The orientation of major axis of the satellites are estimated based on this novel image processing algorithm. Unfortunately, there is no reference about the spin parameters of these derelict satellites (ERS-2,

ALOS-1, SEASAT) to validate this estimation. The derelict satellites such as ENVISAT, Topex/Poseidon, and Ajisai in LEO have a rotational period of 161s, 10.7s, and 2.34s respectively. The rotational period is the time taken by a satellite to complete one full rotation over its axis. ENVISAT was gravity stabilised at the end of its operation, hence it has a relatively higher rotational period whereas Topex/Poseidon and Ajisai are unstable hence it has a low rotational period. The rotational period of each derelict satellite varies and it may depend on the shape (symmetric or asymmetric), size, and altitude of the object. [11]

The ALOS-1, ERS-2, SEASAT, and ISS are imaged for a period of 0.3s and the orientation of the major axis of these derelict satellites has changed rapidly and unstable which are shown in Fig.8, 12, and 16, Whereas the orientation of the major axis of the ISS, has remained relatively stable over the same period. Hence this novel image processing method can distinguish the functional and non-functional objects in LEO. But to estimate the rotation period, spin rate and axis of rotation of non-functional satellite, the target has to be imaged continuously over the entire visible pass (several minutes). [12].

In the future, satellites imaged without motion blur will undergo deconvolution using background stars to accurately estimate the spatial properties of the satellite. This can be achieved in post-processing or using a real-time tip-tilt control system. Finally, the satellite tracking system is required to characterise the object continuously over several minutes, which will provide more information about the derelict satellites.

Acknowledgments

The authors would like to acknowledge and thank the staff at Mt. John University Observatory. This research was supported by the Marsden Fund Contract (MFP UOC1803), administered by the Royal Society of New Zealand.

References

1. McKnight, D., Arora, R., & Winter, R., (2019). Intact Derelict Deposition Study. *First International Orbital Debris Conference*, Texas, USA, 6011.

2. EO portal directory. (2020) About ALOS. [online] https://earth.esa.int/web/eoportal/satellite-missions/a/alos

3. EO portal directory. (2020) About ERS-2. [online] https://directory.eoportal.org/web/eoportal/satellite-missions/e/ers-2

4. EO portal directory. (2020) About SEASAT. [online] https://earth.esa.int/web/eoportal/satellite-missions/s/seasat

5. Hickman, S., Muruganandan, V.A., Clare, R., Weddell, S., (2020). Image metrics for Deconvolution of Satellites in Low Earth Orbit. *IEEE* 978-1-7281-8579.

6. National Aeronautics and Space Administration. (2010) Reference guide to the international space station.[Available]https://www.nasa.gov/pdf/508318main ISS ref guide nov2010.pdf

7. NASA 3D Resources. (2020) ISS (high res). [Online].Available:https://nasa3d.arc.nasa.gov/detail/iss-hi-res

8. Sketchfab. (2021) SEASAT (3d model). [Online]. Available: https://sketchfab.com/3d-models/seasat-05acd7198d60421eb9b9c6ed194d9166

9. Turbosquid. (2021) ERS-2 (3d model). [Online]. Available: https://www.turbosquid.com/3d-models/european-remote-sensing-satellite-max/1028993

10. 3D Warehouse. (2021) ALOS (3d model). [online]. Available:https://3dwarehouse.sketchup.com/search/?q=advanced%20land%20observing%20satellite%20daichi%20alos&searchTab=model

11. Kaminski, K et al., (2017). Determination of Orbital and Spin Parameters of LEO Satellites by Polish and Ukrainian Optical observatories. *7th European Conference on Space Debris*, Darmstadt, Germany.

12. Somers, P., (2011). Cylindrical RSO Signatures, Spin Axis Orientation and Rotation Period Determination. *Advanced Maui Optical and Space Surveillance Technologies Conference*. Wailea, Hawaii